Journal Pre-proof

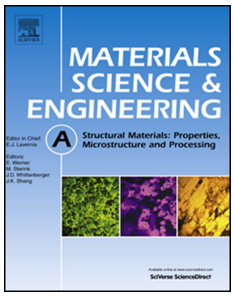

Trimodal shear band nucleation distribution in a Gd-based metallic glass via nanoindentation

M. Gao, J.H. Perepezko

PII: S0921-5093(20)31466-0

DOI: https://doi.org/10.1016/j.msea.2020.140402

Reference: MSA 140402

To appear in: *Materials Science & Engineering A*

Received Date: 25 August 2020

Revised Date: 12 October 2020

Accepted Date: 14 October 2020

Please cite this article as: M. Gao, J.H. Perepezko, Trimodal shear band nucleation distribution in a Gd-based metallic glass via nanoindentation, *Materials Science & Engineering A*, https://doi.org/10.1016/j.msea.2020.140402.

Trimodal shear band nucleation distribution in a Gd-based metallic glass via nanoindentation

M. Gao, J. H. Perepezko*

Department of Materials Science and Engineering, University of Wisconsin-Madison, 1509 University Ave. Madison, WI 53706, USA

Nucleation of shear bands is of critical importance in the deformation behaviors of metallic glasses, but the detailed examination of nucleation kinetics and the correlation with the structure and relaxation kinetics has been few. Here, based upon instrumented nanoindentation with spherical indenter and a great deal of the observed first pop-in events, one unique trimodal distribution of shear band nucleation events in a Gd-based metallic glass was reported. Four different loading rates were employed to study the evolution of the nucleation distribution with external loading. In the analyses of nucleation kinetics, the site density, nucleation rate and activation barrier for three nucleation events were obtained based on the cooperative deformation model, which clearly display the trimodal character. The discovery of a trimodal shear band nucleation distribution provides new insights for understanding the relationship between the heterogeneous structure, relaxation kinetics and deformation mechanism and opportunities for controlling the ductility of amorphous alloys.

Key words: First pop-in events, Shear band, Relaxation, Nanoindentation, Metallic glass

*Corresponding author. Tel.: +1 6082631678. E-mails: perepezk@engr.wisc.edu (Prof. J. H. Perepezko).

1. Introduction

Metallic glasses (MGs) are of great importance in condensed matter physics, materials science and engineering because of their unique structural features and outstanding mechanical, physical and chemical properties [1-4]. As one new member of amorphous materials, One of the enduring attractions of MGs is their interesting and impressive suite of mechanical properties, such as ultrahigh specific strength, ultrahigh hardness, large elastic strain limit, high fracture toughness and unique thermoplastic deformation ability arising from the unique atomic structure without long-range periodic packing order and variable chemical composition [5-8]. However, upon straining at low temperatures (around and lower than the glass transition temperature), MGs usually display a limited macroscopic plastic deformation ability that is accommodated by localized inhomogeneous flow leading to catastrophic fracture, which is the major obstacle for their structural applications [5]. Different from the traditional crystalline alloys that the plastic deformation can be well understood in terms of the generation and motion of dislocation [9-10], the initiation, propagation and interaction of shear bands (SBs) are mainly considered as being responsible for deformation behaviors in MGs [5, 11-12]. The nucleation of SBs in MGs represents the initial plastic yielding and induces a highly localized plastic flow, thus strain softening [5, 11-12]. On the microscopic scale, the nucleation of SBs in MGs is governed by the activation of shear transformation zones (STZs) that represent a localized atomic arrangement and then these STZs percolate, self-organize, and develop into SBs [13-15]. A large plastic deformation level is always accompanied by many SBs whereas for brittle failure only a few SBs are active [12]. Therefore, the easy initiation of SBs appears to be one of the most important factors for large plastic deformability. However, the detailed examination of the SB nucleation kinetics, such as the nucleation rates, the activation barrier and the nucleation site density, and the relationship with the intrinsic structure in MGs has received only limited study [16-18].

For MGs, under an external stress, the initial mechanical response involves local yielding of localized regions (called shear transformation zones, STZs) comprising tens of

atoms that undergo a local structural transformation [5]. Thus, these initial STZs are considered as the nucleation sites for the nucleation and formation of SBs. On the other hand, although the atomic structure for MGs is still under study, many experimental results indicate that MGs are not completely homogeneous at the nanoscale, and there exist viscoelastic defects (also termed as liquid-like regions, weak bonded regions) within the elastic matrix, which exhibit a low modulus, low viscosity and high atomic mobility [19-21]. As the potential nucleation sites of SBs, the STZs are considered to structurally originate from these nanoscale liquid-like regions and different heterogeneous structures lead to different macroscopic mechanical behaviors [15, 22]. Moreover, recent researches reported that a broad spectrum of STZs with a broad range of activation energies exists in MGs and some STZs can even show early activation at a low stress range corresponding to the purely elastic deformation [22-23]. Thus, the potential activated nucleation sites (STZs) are critical for understanding the plastic deformation mechanism in MGs. Meanwhile, it has been reported that there exists one-to-one correspondence between the characteristic relaxation response in terms of the secondary β and faster relaxations and the activated STZs in MGs, which are also closely related to the spatial heterogeneities [24-28]. On this basis, it is hypothesized that the types of SB nucleation sites would be related to the types of characteristic relaxation behavior. Thus, considering the various relaxation behaviors and the heterogeneous structure in MGs [19-21, 29-32], it is expected that there can be multiple rather than a single type of SB nucleation site. Meanwhile, the nucleation process of SBs is a stochastic process considering the random production, annihilation and coalescence of STZs, which is difficult to systematically study by traditional mechanical instruments [5, 15]. Recently, an effective strategy based on the nanoindentation testing was proposed and applied to reveal the bimodal distribution of stochastic SB nucleation events that operate at different stress levels in MGs [33-39]. Based on this strategy, many researchers found that the SB nucleation sites in MGs are bimodal rather than the current view of a single type of site, which is closely related to the local structural heterogeneity [33-39]. In the present work, this approach is applied to explore the possible relation between SB nucleation and relaxation behavior for a ductile Gd-based MG that exhibits three relaxation modes α, β and β' [5, 30, 40] by measuring a series of first

pop-in events. By statistically analyzing the probability distributions of first pop-in load and length with the loading rate of 0.01 mN/s, we found a unique trimodal distribution of SB nucleation sites in this Gd-based MG for the first time. The distributions of first pop-in events for other loading rates also exhibit the similar trimodal character. Finally, the detailed nucleation kinetics including the nucleation sites density, nucleation rate and activation barrier for three nucleation events were determined based on the nucleation theory formalism.

2. Experimental methods

The ingot with the nominal composition of $Gd_{55}Co_{25}Al_{20}$ was prepared by arc melting pure elements and then was remelted five times to ensure homogeneity. The resulting ingot was cast into a copper mold with cyclic cooling water to produce several rod-like samples with the dimensions of 3 × 15 mm (Diameter × Length). The amorphous nature of the samples was confirmed by X-ray diffraction (XRD, Bruker D8 Discovery) and diamond DSC (Perkin Elmer) measurement. A PerkinElmer Diamond DSC instrument was also used to characterize the thermodynamic properties. The elastic properties (the Young's modulus, the shear modulus, the bulk modulus and Poisson's ratio) were measured by MATEC 6600 ultrasonic system.

The dynamical mechanical properties of the $Gd_{55}Co_{25}Al_{20}$ MG sample were measured on a TA Instruments RSA III dynamical mechanical analyzer (DMA) in a nitrogen-flushed atmosphere. The activation energy spectrum including the fast β′ relaxation, slow β relaxation and α relaxation was characterized by the dynamical mechanical properties of the rod-like sample with discrete testing frequency of 1, 2, 4, 8, and 16 Hz.

For nanoindentation tests, the rod-like samples were cut into several thin slices with thickness of about 1 mm. All slices are first mounted into the rubber mold by mixing the epoxy hardener and epoxy resin and then cured for 12 hours. All mounted samples were progressively polished with diamond abrasive films of 30, 15, 6, 3, 1, 0.5 and 0.1 μm. After the initial mechanical polishing, to further obtain a mirror surface with nano-scale roughness, we applied an additional final polishing stage using colloidal silica (one chemo-mechanical

polish procedure, and it combines the effect of mechanical polishing with etching). Finally, to further exclude the effect of the surface residual stress on the nanoindentation tests, all of the above polished samples were held at room temperature for at least three weeks to relax the surface residual stress.

To detect the first pop-in events (corresponding to SB nucleation), a series of the nanoindentation tests during loading were conducted on a Hysitron TI950 (Bruker) nanoindenter equipped with a spherical tip (the effective radius of the tip is about 1.10 μm). All tests were conducted in a load-controlling mode at four constant loading rates of 0.01, 0.05, 0.2 and 1 mN/s. For each loading rate, more than 200 repeats were performed to ensure that the results are statistically significant. To prevent the possible overlapping of strain fields between the neighboring indentations, we designed a 20 μm spacing distance between the neighboring loading points within the rectangular matrix.

3. Results and discussions

3.1. Characterization of thermodynamic and dynamic properties for $Gd_{55}Co_{25}Al_{20}$ MG

Fig. 1(a) displays a typical heat flow curve for $Gd_{55}Co_{25}Al_{20}$ MG and the glass transition and the following primary crystallization take place during heating. The detailed values of the thermodynamic properties such as the glass transition temperature and primary crystallization temperature are listed in Table 1. The inserted XRD plot verifies the amorphous nature for the as-cast sample. Fig. 1(b) shows the loss modulus with the increase of the temperature for $Gd_{55}Co_{25}Al_{20}$ MG samples and the applied DMA frequency and the heating rate is 1 Hz and 5 K/min, respectively. It is evident that the curve of the loss modulus and temperature exhibits three distinct peaks within the testing temperature range: The main α relaxation peak corresponding to the glass transition appears at 616 K and the following secondary β relaxation takes place at 476 K; before α relaxation and β relaxation, there exists the third relaxation event at a lower temperature of 279 K (called the fast β' relaxation), which are consistent with the previous research [30]. The inserted plot of Fig. 1(b) gives the evolution of the temperature peaks (T_β and $T_{\beta'}$) corresponding to β' relaxation and β relaxation with

different frequencies *f*. One can see that both of the temperature peaks for β' relaxation and β relaxation shift to higher temperatures with the increase of the applied frequency. Thus, the activation energies of β relaxation and β' relaxation (E_β and $E_{\beta'}$) can be calculated based on the Arrhenius equation ($\ln(f) = Constant + \frac{E}{R}(\frac{1}{T})$). And the detailed values of E_β and $E_{\beta'}$ are also listed in Table 1.

3.2. Statistical analysis of the load and length of first pop-in events with the loading rate of 0.01 mN/s

A typical nanoindentation load-displacement curve with a loading rate $\dot{p}$ of 0.01 mN/s is shown in Fig. 2(a). For nanoindentation, the materials initially follow an elastic Hertzian response, as marked by the red curve in Fig. 2(a). The termination of the elastic response is indicated by a pop-in event where there appears a sudden increase in displacement at a constant load marked by blue dashed circle in Fig. 2(a). Previous research has confirmed that the first pop-in event corresponds to the initiation of a SB [33]. Thus, to investigate the SB nucleation kinetics of Gd-based MG, we focus on these first pop-in events. Based on about 200 individual nanoindentation measurements in one sample, the distributions of the load and the length of the first pop-in events are separately shown in Fig. 2(b) and Fig. 2(c). It is evident that there is no systematic drift over the whole test course and the data is uncorrelated, which indicates that SB nucleation is a stochastic process [32-33]. Then, the cumulative distribution and probability distribution of the first pop-in load and length can be obtained in Fig. 2(d) and the insertions of Fig. 2(d). From Fig. 2(d), it is obvious that the probability distributions for the first pop-in load and length display three peaks, which indicates that there exists multiple SB nucleation events. For the statistical analysis of the experimental data, the obtained probability distribution function can be fitted by a Gaussian function or the Weibull function [33-35, 37]. First, the probability distributions of the first pop-in load and length can be well fitted by three Gaussian functions, which clearly displays a trimodal behavior. What is more, the fitting results by two and four Gaussian functions were also conducted and were shown in Figs. S1(a)-S1(f) of Supplementary Materials. It is evident that

the fitting results by three Gaussian functions are the best and the values of the R-square error are 0.99, which confirms the trimodal nature of SB sites in Gd-based MG. Secondly, we applied the Weibull functions to fit the experimental data and the detailed fitting results can be seen in Figs. S2(a)-S2(h) of Supplementary Materials. From Figs. S2(a)-S2(b) and S2(e)-S2(f), the use of only one and two Weibull functions cannot fit the experimental results well (the standard error are 0.53 and 0.84, 0.62 and 0.82,). In contrast, the probability distributions can be well fitted by three Weibull functions, as shown in Figs. S2(c) and S2(g). Moreover, we can see that four Weibull functions cannot give better fitting results in Figs. S2(d) and S2(h). Thus, from the above analyses and results, the probability distributions for the first pop-in length and load can be well fitted by three Gaussian or Weibull functions, which displays the trimodal character of SB nucleation. Each Gaussian or Weibull function represents one nucleation site and there actually exist three different SB nucleation sites in the Gd-based MG. Due to the equivalence of fit to the distribution data by the Gaussian and Weibull functions, the following discussion is based upon the use of the Gaussian function analysis. The corresponding nucleation sites are named site A (low-load mode), B (medium-load mode) and C (high-load mode), respectively. To clearly display the trimodal character of the SB nucleation events, a three-dimensional probability distribution map and the corresponding two-dimensional probability distribution projection of the load and length at first pop-in events are exhibited in the upper and lower parts of Fig. 3. Three maxima of the probability distribution for SB nucleation events can be identified from Fig. 3.

3.3. Loading rate effect on the probability distribution of first pop-in events load and length

To examine the loading rate effect on SB nucleation, additional three loading rates of 0.05, 0.2 and 1 mN/s were applied, and the corresponding cumulative density distributions are plotted in Fig. 4(a). A clear shift of the distributions to higher load range can be observed when the loading rate increases from 0.01 mN/s to1 mN/s, which is consistent with the previous research [34]. From Fig. 4(a), the corresponding three-dimensional probability density distributions can be obtained and are shown in Fig. 4(b). For all loading rates, the probability density curves can be clearly decomposed into three Gaussian functions

corresponding to the three nucleation events in Fig. 4(b). Based on the distribution spectra in Fig. 4(b), the load peak value p_m evolution of the probability density with loading rates for each nucleation site can be obtained and is shown in Fig. 4(c). With the increase of loading rate, it is evident that the peak load values for all three sites increase, which indicates that the activation loads for all three nucleation sites increase with the loading rate. Moreover, by fitting the linear empirical equation of $p_m = a + b\log(\dot{p})$, the values of the loading rate sensitivity factor b can be calculated as shown in the insertion of Fig. 4(c). The low-load site A exhibits the highest loading rate sensitivity and the high-load site C has the lowest loading rate sensitivity. To further display the evolution paths with load and loading rate for three nucleation sites, a map of the governing nucleation site can be plotted by obtaining the transition loads from site A to site B (blue empty squares) and from site B to site C (red empty circles) in Fig. 4(b), as shown in Fig. 4(d). The low-load site A lies in lower right region with the low load and high loading rate, and the high-load site C controls the low loading rate and high load region, which is consistent with the above evolution of the probability density for three nucleation sites in Fig. 4(b). It is worthwhile noting that in previous work a bimodal distribution of first pop-in events was observed in four different MGs during nanoindentation with a 5 μm spherical indenter radius and a loading rate of 0.07 mN/s [37]. Similar bimodal distributions were reported by Wang and Perepezko [33] on two MGs with an indenter radius of 2.5 μm and the loading rate ranging from 0.05 to 2 mN/s and by Zhao et al [36] on eight MGs with an indenter radius of 2 μm and loading rates between 1.1 and 4.76 mN/s. The tendency for the development of a bimodal distribution of pop-in events has been attributed to the use of a large radius indenter and high loading rates [37]. However, in the current work the indenter radius employed was 1.1 μm and the loading rate ranges from 0.01 to 1.0 mN/s, which are smaller than those used in previous studies. Thus, the development of a trimodal distribution of first pop-in events is not consistent with the claim that the multimodal distributions are favored by large indenter radius and high loading rates, which indicates that the multimodal distributions of SB nucleation behaviors may be a universal character in MGs.

3.4. SB nucleation kinetics analyses-site density

For MGs, under external loading, the potential SB nucleation sites can be activated and then these activated SB nucleation sites cooperate together and form into the SB. For the formation of SB, one physical scheme was proposed and was shown in Fig. 5(a). For the SB nucleation kinetics in MGs, the nucleation site density is a critical parameter that determines the final density of the SBs governing the macroscopic plasticity, and the transition of the deformation mechanism between inhomogeneous deformation and homogeneous flow [5]. Thus, it is necessary to investigate the evolution of the nucleation site density for three nucleation sites with external load. Here, for simplicity, it is assumed that the activated nucleation sites are randomly distributed in the deformed volume V_{def}. For the deformation volume at an external load under the nanoindenter tip, it usually follows the minimum criteria for a pop-in event. And the site density m is the ratio of the number of density and the deformed volume under nanoindenter. Thus, the nucleation site probability X can be expressed by [5]

$$X = 1 - \exp(-mV_{def}) \quad (1),$$

The value of V_{def} is usually taken as about 1%V_{dis}, where V_{dis} is the volume displaced beneath the spherical nanoindenter [32-33]. The V_{dis} can be taken as

$$V_{dis} = \frac{\pi}{6}\left[3\left(\frac{9P^2{R_i}^5}{16{E_r}^2}\right)^{1/3} + \frac{9P^2}{16{E_r}^2 R_i}\right] \quad (2),$$

where P is the external load, R_i is the radius of the spherical nanoindenter, E_r is the reduced elastic modulus, $E_r = \frac{E_s E_i}{E_i(1-{\nu_s}^2)+E_s(1-{\nu_i}^2)}$ [32-33] (the detailed values can be seen in Table 1). For the experimental values of X, the values for the low-load, medium load and high-load mode are determined based on the fraction of the total nucleation events with a given load in the previous fitted probability distribution curves with three peaks in Fig. 4(b). Thus, the detailed site densities of low-load, medium load and high-load modes can be obtained by

$$m = -\frac{1}{0.01\frac{\pi}{6}[3\left(\frac{9P^2{R_i}^5}{16{E_r}^2}\right)^{1/3} + \frac{9P^2}{16{E_r}^2R_i}]}\ln(1-X) \quad (3).$$

Based upon the trimodal probability density functions in Fig. 4(b), an independent evaluation of the nucleation site density for each loading rate can be derived in Fig. 5(b). From Fig. 5(b), all of the nucleation site density curves for all four loading rates can be decomposed into three Gaussian functions corresponding to three nucleation sites, which is similar to the probability density curves in Fig. 4(b). What is more, one can see that three nucleation sites display the maximum site density within different load ranges in Fig. 5(b). This result directly indicates that three nucleation sites control the nucleation process within different load ranges during continuous nanoindentation loading, which is consistent with the results in Fig. 4(d).

3.5. SB nucleation kinetics analyses-Nucleation rate and nucleation barrier

The nucleation rate and the activation barrier with external load for different loading rates can be obtained based on the Johnson-Samwer cooperative deformation model [14]. In order to extract the nucleation rate from the experimental first pop-in distributions, we introduced the kernel density corresponding to the experimental probability density function (*f(t)*). Then, by integrating the fitted curve $f(t)$ from the experimental data, one can calculate the cumulative distribution function $F(t)$. Based on the obtained probability and cumulative functions $f(t)$ and $F(t)$, the statistically probability function called hazard rate function $\lambda(t)$ can be expressed as $\lambda(t) = f(t)/(1 - F)$. The hazard function $\lambda(t)$ indicates that a specimen can survive up until time t during one SB nucleation event. Finally, the nucleation rate J is directly related to the hazard function by $J = \lambda/V_{def}$, where V_{def} is the deformation volume at a given load and is about $0.01V_{dis}$ (V_{dis} can be seen by Eq. (2)). Thus, under four loading rates, the detailed SB nucleation rate for three nucleation sites can be obtained and be shown in Fig. 6.

Based on the cooperative shear deformation model proposed by W. L. Johnson and K. Samwer [14], considering that the SB nucleation can be considered as an activation process by the external load, the nucleation rate J can be expressed as

$$J = \omega \exp\left(-\frac{\Delta W(\tau)^*}{kT}\right) \quad (4)$$

where $\Delta W(\tau)^*$ is the activation barrier for SB nucleation and it is a function of the shear stress τ; ω is the frequency constant and it is the product of an atomic jump frequency (for MGs, it can be taken as 10^{13} s^{-1}) and the nucleation site density. Thus, from Eq. (4), we can get

$$\Delta W(\tau)^*/kT = \ln(\omega/J) \quad (5)$$

Then, based on the calculated nucleation rates in Fig. 6, we can determine the activation barriers for different loading rates, as shown in Fig. 7. From the insertion of Fig. 6(a), the resultant nucleation rate for 0.05 mN/s as a function of load can be separated into three discrete curves corresponding to three nucleation sites. The same analysis can be conducted for the other three loading rates and the similar results were also exhibited in Figs. 6(b)-6(d). Then, from Fig. 7(a), the resultant activation barrier W/kT (at room temperature 300 K) for 0.05 mN/s as a function of load can be obtained and shown in the insertion of Fig. 7(a). This curve can also be separated into three discrete curves corresponding to three nucleation sites. Meanwhile, for different nucleation sites, with the increase of the external load, the activation barriers for all sites display the descending trend. Similarly, the analyses for the other three loading rates are also conducted, as shown in Figs. 7(b)-7(d). It has been reported that the plastic flow in MGs can be considered as the consequence of stress-induced glass transition and the effect of the external stress is to reduce the apparent activation energy barrier in the local energy landscape and to reduce viscosity, thereby changing a glass into a liquid [14, 42]. Thus, the activation of the SB nucleation sites can be considered as a local stress-induced glass transition event and the activation energy should decrease with the increase of load, which is consistent with our results.

3.5. Correlation between SB nucleation sites and typical relaxation events in Gd-based MG

Previous researches have indicated that there exists an intrinsic relationship between the activation of STZs and β relaxations in MGs, and the activation energies of β relaxations and the barriers of STZs are nearly equivalent [24-25]. Thus, to investigate the possible

correlation between the SB nucleation sites and the relaxation events, it is necessary to compare the SB nucleation barrier without load W_0 with the activation energy for relaxation events. From the inserted plot of Fig. 7(a), the W_0 for site A, B and C can be obtained by extrapolating the fitted curves and the detailed values are 113, 74 and 57 kJ/mol. In contrast, the activation energies of slow β relaxation E_β and fast β' relaxation $E_{\beta'}$ for Gd-based MG have been obtained in Fig. 1(b) and the detailed values are 113±5 and 54±5 kJ/mol. Similarly, the values of W_0 for other three loading rates can also be determined based on Figs. 7(b)-7(d) and are listed in Table 2. And the W_0 with the loading rates was shown in Fig. 8(a). First, it is noted that W_0 for three nucleation sites is an intrinsic parameter and it should be independent on the loading rates, which is consistent with our results in Table 2. Secondly, it is interesting to notice: the nucleation barrier of the high load modes-site C is close to the activation energy of fast β' relaxation and the nucleation barrier of low load mode-site A is close to the activation energy of slow β relaxation.

For the typical relaxation events in Rare earth-based MGs, such as the secondary β relaxation and fast β' relaxation, many researchers have revealed that the fast β' relaxations originate from an individual local flow event (it usually behaves the cage-breaking event), and the secondary β relaxations are activated by the connection of many local flow events exhibiting the 'string-like' configurations [27-28, 30, 32, 42-44]. Therefore, based on the above results of the calculated nucleation barriers and the relaxation events, the physical mechanism for the activation of three different SB nucleation sites in the Gd-based MG can be proposed. There exist many nano-scale liquid-like structural heterogeneities in Gd-based MG and they are the potential nucleation sites for SB formation. Under different external load ranges, these heterogeneities exhibit three different activation configurations. First, in the low load range, these heterogeneities are prone to be activated by the 'string-like' configurations considering that the activation energy is very close to the secondary β relaxation, which corresponds to the activation of site A. Second, in the high load ranges, these heterogeneities are prone to be activated by 'cage-breaking' events considering that the activation energy is very close to the fast β' relaxation, which

corresponds to the activation of site C. Finally, in the medium load range, the activation process for SB nucleation appears to differ from the single β or β' relaxation modes. Considering that the activation barrier range for site B is between the activation barrier of site A and the activation barrier of site C, the heterogeneities may be prone to be activated by the new combined configuration of the 'cage-breaking' and 'string-like' in the medium load range, which requires further investigation to clarify the mechanism. Therefore, based on the above results of activation barriers for three nucleation sites, one simple physical image of the physical mechanism for the activation of the trimodal SB nucleation sites in Gd-based MG can be drawn and shown in Fig. 8(b). In addition, considering that the 'string-like' configurations will likely show a more viscoelastic behavior and the 'caging' atomic configuration deforms more rigidly like an elastic spring [27-28, 30, 32, 42-44], the nucleation behaviors such as the first pop-in load for site A exhibits a relatively strong strain rate dependence, while the site B and site C have a weak strain rate dependence in Fig. 3c.

4. Conclusions

In conclusion, we reveal a unique trimodal distribution of SB nucleation events in a $Gd_{55}Co_{25}Al_{10}$ MG by statistically analyzing about 200 first pop-in events during continuous-loading nanoindentation tests. A three-dimensional mapping of probability density distribution and the corresponding two-dimensional projection of first pop-in load and length are obtained, which clearly displays the trimodal character. The nucleation site density, the nucleation rate and the activation barrier for three nucleation sites were calculated based on the cooperative deformation model. These results have identified the activation of SB nucleation sites and the typical relaxations are directly related in Gd-based MGs. The discovery of a trimodal distribution of shear band nucleation events provides insight for understanding the relationship between the heterogeneous structure, relaxation kinetics and deformation mechanism. It also offers opportunities for promoting nucleation to enhance SB activity and then controlling the ductility of amorphous alloys.

Data availability

The raw/processed data required to reproduce these findings cannot be shared at this time as the data also forms part of an ongoing study.

Declaration of competing interest

The authors declare that they have no known competing financial interests or personal relationships that could have appeared to influence the work reported in this paper.

Acknowledgements

M. Gao and J. H. Perepezko acknowledge the financial support from the Office of Naval Research (N00014-16-1-2401, N00014-20-1-2704). Valuable discussions with Dr. W. Kim and experimental assistances from J. Morasch and L. A. Turner are greatly appreciated.

CRediT author statement

Meng Gao: Conceptualization, Methodology, Investigation, Data curation, Software, Validation, Visulatzation, Writing- Original Draft Preparation. John H. Perepezko: Conceptualization, Supervision, Writing- Reviewing and Editing.

References

[1] M. W. Chen, A brief overview of bulk metallic glass, NPG Asia Mater. 3 (2007) 82-90.

[2] W. H. Wang, C. Dong, C. H. Shek, Bulk metallic glasses, Mater. Sci. Eng. Rep. 44 (2004) 45–89.

[3] M. Telford, The case of bulk metallic glass, Mater. Today 7 (2004) 36-43.

[4] J. Schroers, Bulk metallic glasses, Phys. Today 66 (2013) 32-37.

[5] C. A. Schuh, T. C. Hufnagel, U. Ramamurty, Mechanical behavior of amorphous alloys, Acta Mater. 55 (2007) 4067-4109.

[6] M. D. Demetriou, M. E. Launey, G. Garrett, J. P. Schramm, D. C. Hofmann, W. L. Johnson, R. O. Ritchie, A damage-tolerant glass, Nat. Mater. 10 (2011) 123-128.

[7] S. V. Madge, A. Caron, R. Gralla, G. Wilde, S. K. Mishra, Novel W-based metallic glass with high hardness and wear resistance, Intermetallics 47 (2014) 6-10.

[8] J. Schroers, Processing of bulk metallic glass, Adv. Mater. 22 (2010) 1566-1597.

[9] J. P. Hirth, J. Lothe, Theory of Dislocations, John Wiley and Sons, Inc., 1982.

[10] W. Blum, Discussion: Activation volumes of plastic deformation of crystals, Scr. Mater. 146 (2018) 27-30.

[11] A. Inoue, A. Takeuchi, Recent development and application products of bulk glassy alloys, Acta Mater. 59 (2011) 2243-2267.

[12] A. L. Greer, Y. Q. Cheng, E. Ma, Shear bands in metallic glasses, Mater. Sci. Eng. Rep. 74 (4) (2013) 71–132.

[13] J. S. Langer, Shear-transformation-zone theory of deformation in metallic glasses, Scr. Mater. 54 (2006) 375-379.

[14] W. L. Johnson, K. Samwer, A universal criterion for plastic yielding of metallic glasses with a $(T/T_g)^{2/3}$ temperature dependence, Phys. Rev. Lett. 95 (2005) 195501.

[15] D. Sopu, A. Stukowski, M. Stoica, S. Scudino, Atomic-level processes of shear band nucleation in metallic glasses, Phys. Rev. Lett. 119 (2017) 195503.

[16] D. Klaumünzer, A. Lazarev, R. Maaß, F. H. Dalla Torre, A. Vinogradov, J. F. Löffler, Probing shear-band initiation in metallic glasses, Phys. Rev. Lett. 107 (2011) 185502.

[17] C. A Schuh, A. C. Lund, Application o nucleation theory to the rate dependence of incipient plasticity during nanoindentation, J. Mater. Res. 19(7) (2004) 2152-2158.

[18] L. Wang, Z. P. Lu, T. G. Nieh, Onset of yielding and shear band nucleation in a Au-based bulk metallic glass, Scr. Mater. 65 (9) (2011) 759-762.

[19] J. C. Ye, J. Lu, C. T. Liu, Q. Wang, Y. Yang, Atomic free-volume zones and inelastic deformation of metallic glasses, Nat. Mater. 9 (2010) 619-623.

[20] H. Wagner, D. Bedorf, S. Kuchemann, M. Schwabe, B. Zhang, W. Arnold, K. Samwer, Local elastic properties of a metallic glass, Nat. Mater. 10 (2011) 439-442.

[21] P. Tsai, Kelly Kranjc, K. M. Flores, Hierarchical heterogeneity and an elastic microstructure observed in a metallic glass alloy, Acta Mater. 139 (2017) 11-20.

[22] J. D. Ju, M. Atzmon, A comprehensive atomic analysis of the experimental dynamic-mechanical response of a metallic glass, Acta Mater. 74 (2014) 183-188.

[23] R. Maaβ, K. Samwer, W. Arnold, C. A. Volkert, A single shear band in a metallic glass: Local core and wide soft zone, Appl. Phys. Lett. 105 (2014) 171902.

[24] H. B. Yu, W. H. Wang, H. Y. Bai, Y. Wu, M. W. Chen, Relating activation of shear transformation zones to β relaxations in metallic glasses, Phys. Rev. B 81 (2010) 220201 (R).

[25] L. N. Hu, Y. Z. Yue, Secondary relaxation in metallic glass formers: Its correlation with the genuine Johari-Goldstein relaxation, J. Phys. Chem. C 113 (2009) 15001.

[26] J. C. Qiao, X. D. Liu, Q. Wang, C. T. Liu, J. Lu, Y. Yang, Fast secondary relaxation and plasticity initiation in metallic glasses, Natl. Sci. Rev. 5 (2018) 616-618.

[27] F. Zhu, H. K. Nguyen, S. X. Song, Daisman P. B. Aji, A. Hirata, H. Wang, K. Nakajima, M. W. Chen, Intrinsic correlation between β-relaxation and spatial heterogeneity in a metallic glass, Nat. Comm. 7 (2016) 11516.

[28] D. P. Wang, J. C. Qiao, C. T. Liu, Relating structural heterogeneity to β relaxation processes in metallic glasses, Mater. Res. Lett. 7 (2019) 305-311.

[29] H. B. Yu, W. H. Wang, K. Samwer, The β relaxation in metallic glasses: an overview, Mater. Today 16 (2013) 183-191.

[30] L. Z. Zhao, R. J. Xue, Z. G. Zhu, K. L. Ngai, W. H. Wang, H. Y. Bai, A fast dynamic mode in rare earth based glasses, J. Chem. Phys. 144 (2016) 204507.

[31] S. Kuchenmann, R. Maaβ, Gamma relaxation in bulk metallic glasses, Scr. Mater. 137 (2017) 5-8.

[32] Q. Wang, S. T. Zhang, Y. Yang, Y. D. Dong, C. T. Liu, J. Lu, Unusual fast secondary relaxation in metallic glass, Nat. Comm. 6 (2015) 7876.

[33] J. H. Perepezko, S. D. Inhoff, M. W. Chen, J. Q. Wang, S. Gonzalez, Nucleation of shear bands in amorphous alloys, Proc. Natl. Acad. Sci. U. S. A. 111 (2014) 3938-3942.

[34] D. Tonnies, K. Samwer, P. M. Derlet, C. A. Volkert, R. Maaβ, Rate-dependent shear-band initiation in a metallic glass, Appl. Phys. Lett. 106 (2015) 171907.

[35] J. Q. Wang, J. H. Perepzko, Focus: Nucleation kinetics of shear bands in metallic glass, J. Chem. Phys. 145 (2016) 211803.

[36] X. N. Zhao, Q. P. Cao, C. Wang, X. D. Wang, D. X. Zhang, S. X. Qu, J. Z. Jiang, Dependence of room-temperature nanoindentation creep behavior and shear transformation zone on the glass transition temperature in bulk metallic glasses, J. Non-Cryst. Solids 445-446 (2016) 19-29.

[37] Shankha Nag, R. L. Narayan, Jae-il Jang, C. Mukhopadhyay, U. Ramamurty, Statistical nature of the incipient plasticity in amorphous alloys, Scr. Mater. 187 (2020) 360-365.

[38] In-Chul Choi, Yakai Zhao, Byung-Gil Yoo, Yong-Jae Kim, Jin-Yoo Suh, U. Ramamurty, Jae-il Jang, Estimation of the shear transformation zone size in a bulk metallic glass through

statistical analysis of the first pop-in stresses during spherical nanoindentation, Scr. Mater. 66 (2012) 923-926.

[39] In-Chul Choi, Yakai Zhao, Yong-Jae Kim, Byung-Gil Yoo, Jin-Yoo Suh, U. Ramamurty, Jae-il Jang, Indentation size effect and shear transformation zone size in a bulk metallic glass in two different structural states, Acta Mater. 60 (2012) 6862-6868.

[40] S. Li, R. J. Wang, M. X. Pan, D. Q. Zhao, W. H. Wang, Formation and properties of RE55Al25Co20 (RE = Y, Ce, La, Pr, Nd, Gd, Tb, Dy, Ho and Er) bulk metallic glasses, J. Non-Cryst. Solids 354 (2008) 1080-1088.

[41] P. Luo, Z. Lu, Y. Z. Li, H. Y. Bai, P. Wen, W. H. Wang, Probing the evolution of slow flow dynamics in metallic glasses, Phys. Rev. B 93 (2016) 104204.

[42] P. F. Guan, M. W. Chen, T. Egami, Stress-temperature scaling for steady-state flow in metallic glasses, Phys. Rev. Lett. 104 (2010) 205701.

[43] Z. G. Zhu, Y. Z. Li, Z. Wang, X. Q. Gao, P. Wen, H. Y. Bai, K. L. Ngai, W. H. Wang, Compositional origin of unusual β-relaxation properties in La-Ni-Al metallic glasses, J. Chem. Phys. 141 (2014) 084506.

[44] Z. G. Zhu, Z. Wang, W. H. Wang, Binary rare earth element-Ni/Co metallic glasses with distinct β-relaxation behaviors, J. Appl. Phys. 118 (2015) 154902.

Figure and table captions

Fig. 1. (a) Heat flow curve for the as-cast $Gd_{55}Co_{25}Al_{20}$ MG sample with the heating rate of 20 K/min. The inserted plot shows the amorphous nature for the as-cast sample by XRD. (b) Temperature dependence of the loss modulus at testing frequency of 1 Hz and the heating

rate of 5 K/min. The blue, red, and the magenta curves are guides for three relaxation peaks. The inserted plot gives the activation energies for β relaxation and β' relaxations.

Fig. 2. (a) One typical nanoindentation displacement-load plot with two pop-in events. The black curves are the experimental data with a loading rate of 0.01 mN/s, the blue dashed circle marks the first pop-in event and the red curve is the fitting curve by Hertzian elastic contact theory. (b) The load distribution at first pop-in events for about 200 tests. (c) The length distribution at first pop-in events for about 200 tests. (d) Cumulative count distribution of first pop-in load and length. The inserted plots give the corresponding probability distributions of first pop-in load and length.

Fig. 3. Trimodal distribution of first pop-in events in Gd-based MG: (Up) Three-dimensional wiremesh mapping as a function of load and length at first pop-in events; (Down) Corresponding two-dimensional projection with first pop-in load and length.

Fig. 4. (a) Cumulative distributions of first pop-in load for four loading rates. (b) Three-dimensional probability density curves for four loading rates. Three separate Gaussian plots for each loading rate stand for three different SB nucleation modes. (c) Plot of load peak values of the fitting Gaussian curves for three nucleation sites in Fig. 4(b) and loading rate. (d) Mapping of three nucleation sites for different first pop-in loads and loading rates.

Fig. 5. (a) Scheme of the SB formation based on the activation and connection of the potential nucleation sites. (b) Three dimensional of the site densities for three SB nucleation sites versus load and loading rates.

Fig. 6. (a) SB nucleation rate and load with four different loading rates. The inserted plot gives the nucleation rate with load under the loading rate of 0.05 mN/s and the detailed fitting curves corresponding to three nucleation sites. (b) The nucleation rate with load under the loading rate of 0.01 mN/s and the detailed fitting curves corresponding to three nucleation sites. (c) The nucleation rate with load under the loading rate of 0.2 mN/s and the detailed fitting curves corresponding to three nucleation sites. (d) The nucleation rate with load under

the loading rate of 1 mN/s and the detailed fitting curves corresponding to three nucleation sites.

Fig. 7. (a) SB nucleation activation barrier and load with four different loading rates. The inserted plot gives the nucleation activation barrier with load under the loading rate of 0.05 mN/s and the detailed fitting curves corresponding to three nucleation sites. (b) The nucleation activation barrier with load under the loading rate of 0.01 mN/s and the detailed fitting curves corresponding to three nucleation sites. (c) The nucleation activation barrier with load under the loading rate of 0.2 mN/s and the detailed fitting curves corresponding to three nucleation sites. (d) The nucleation activation barrier with load under the loading rate of 1 mN/s and the detailed fitting curves corresponding to three nucleation sites.

Fig. 8. (a) Activation barrier range for three nucleation sites with different loading rates. The activation energies for slow β and fast β' relaxation for Gd-based MG are exhibited. (b) Scheme of the relationship between the structural heterogeneity, the activation of SB nucleation sites and SB formation.

Table 1. Summary of physical parameters for $Gd_{55}Co_{25}Al_{20}$ MG sample in this work and the experimental parameters for the instrumental nanoindenter. $Gd_{55}Co_{25}Al_{20}$ MG sample: Glass transition temperature T_g, primary crystallization temperature T_{x1}, Young's modulus E_s, shear modulus G_s, bulk modulus K_s, Poisson's ratio υ_s, reduced elastic modulus E_r. Nanoindenter: Young's modulus E_i, Poisson's ratio υ_i, the radius of the tip R_i. The reduced elastic modulus can be calculated by $E_r = \frac{E_s E_i}{E_i(1-\upsilon_s 2)+E_s(1-\upsilon_i 2)}$.

Table 2. The values of the nucleation barrier W_0 without load for three nucleation sites in Gd-based MG. The values of W_0 are obtained by extrapolating the fitted curves into the external load of 0, as shown in the inserted plot of Fig. 7(a), and Figs. 7(b)-7(d).

Figures

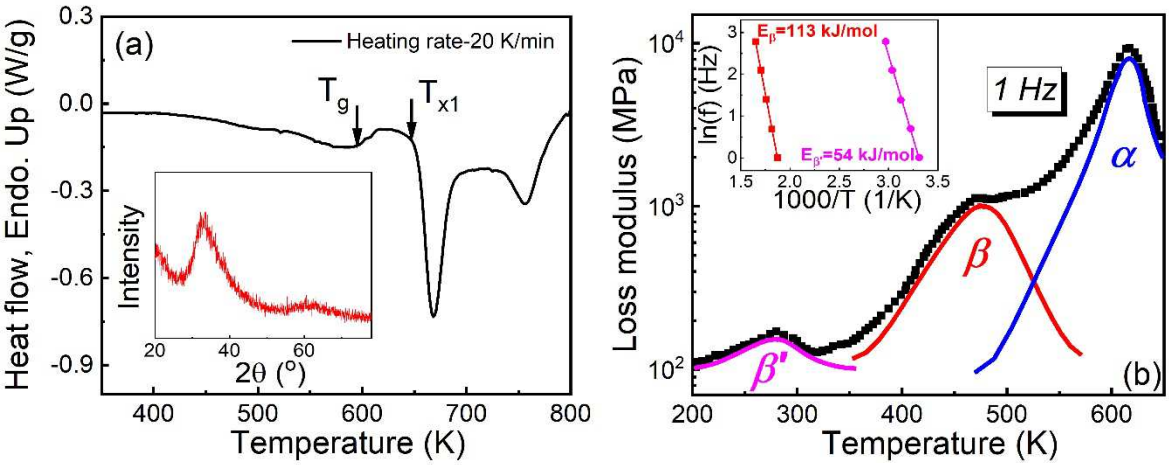

Fig. 1. ***M. Gao et al.***

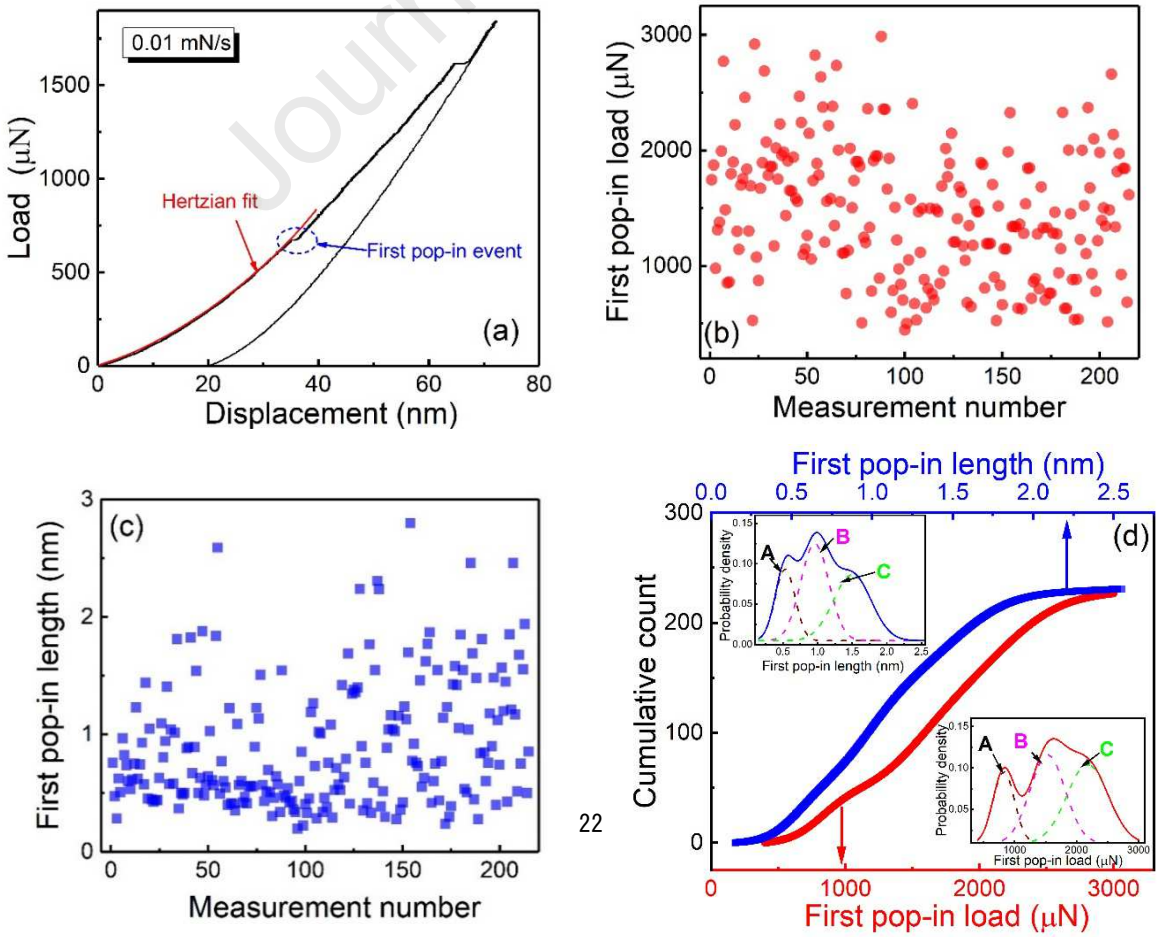

Fig. 2. ***M. Gao et al.***

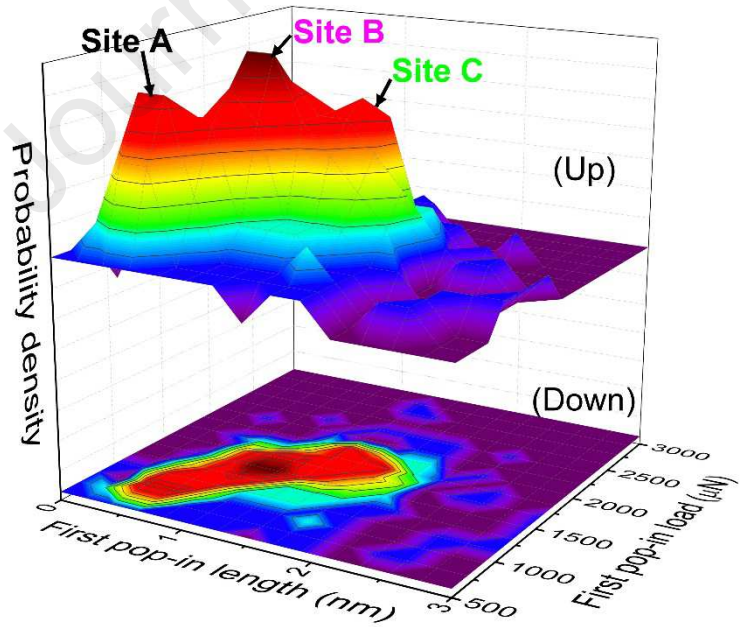

Fig. 3. ***M. Gao et al.***

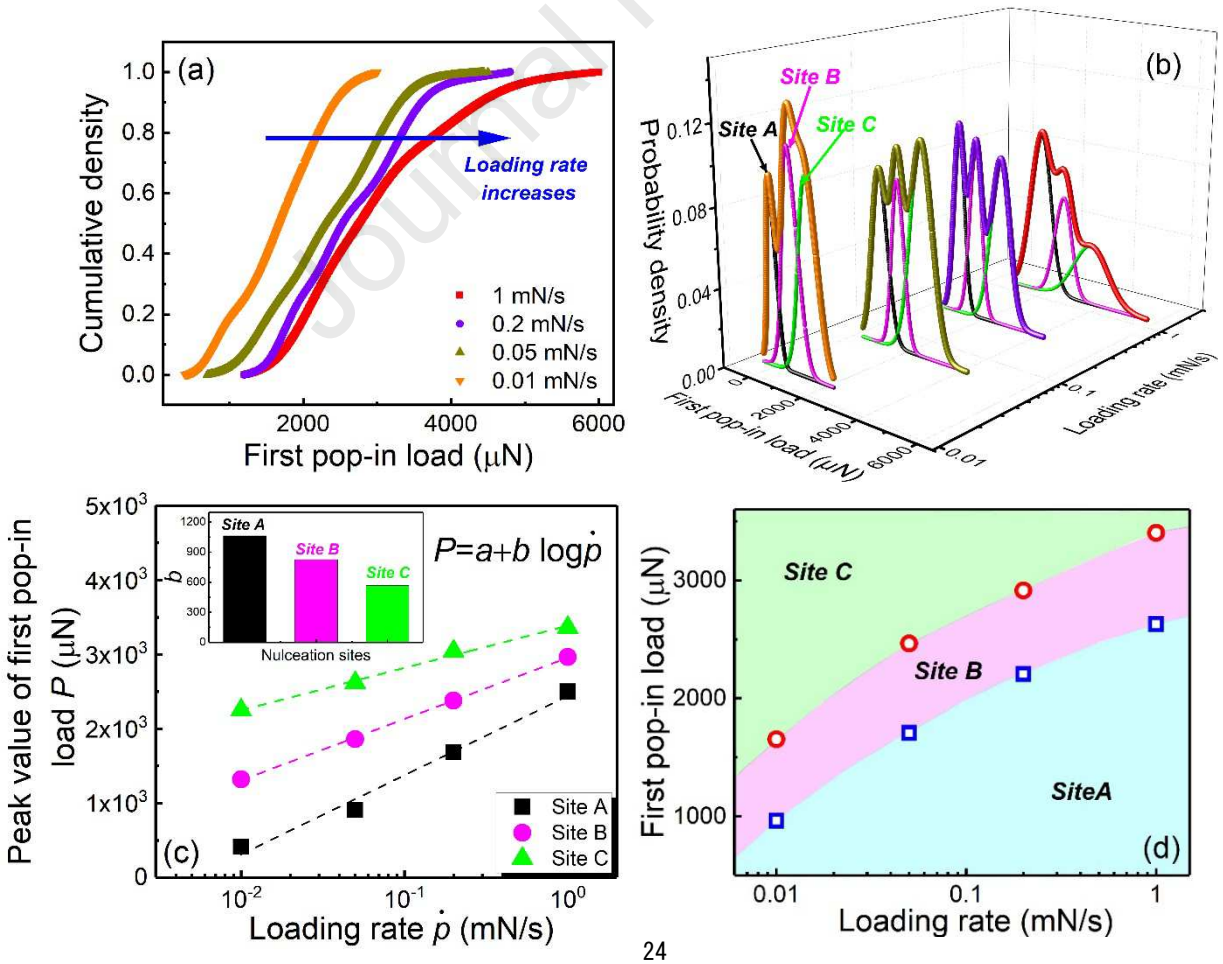

Fig. 4. ***M. Gao et al.***

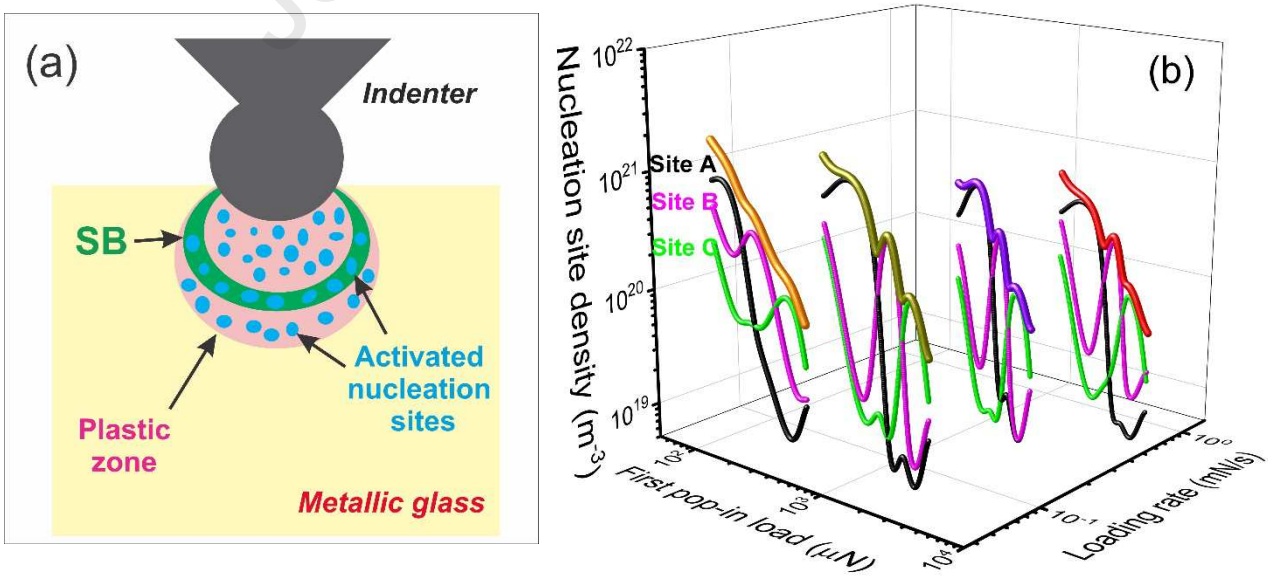

Fig. 5. ***M. Gao et al.***

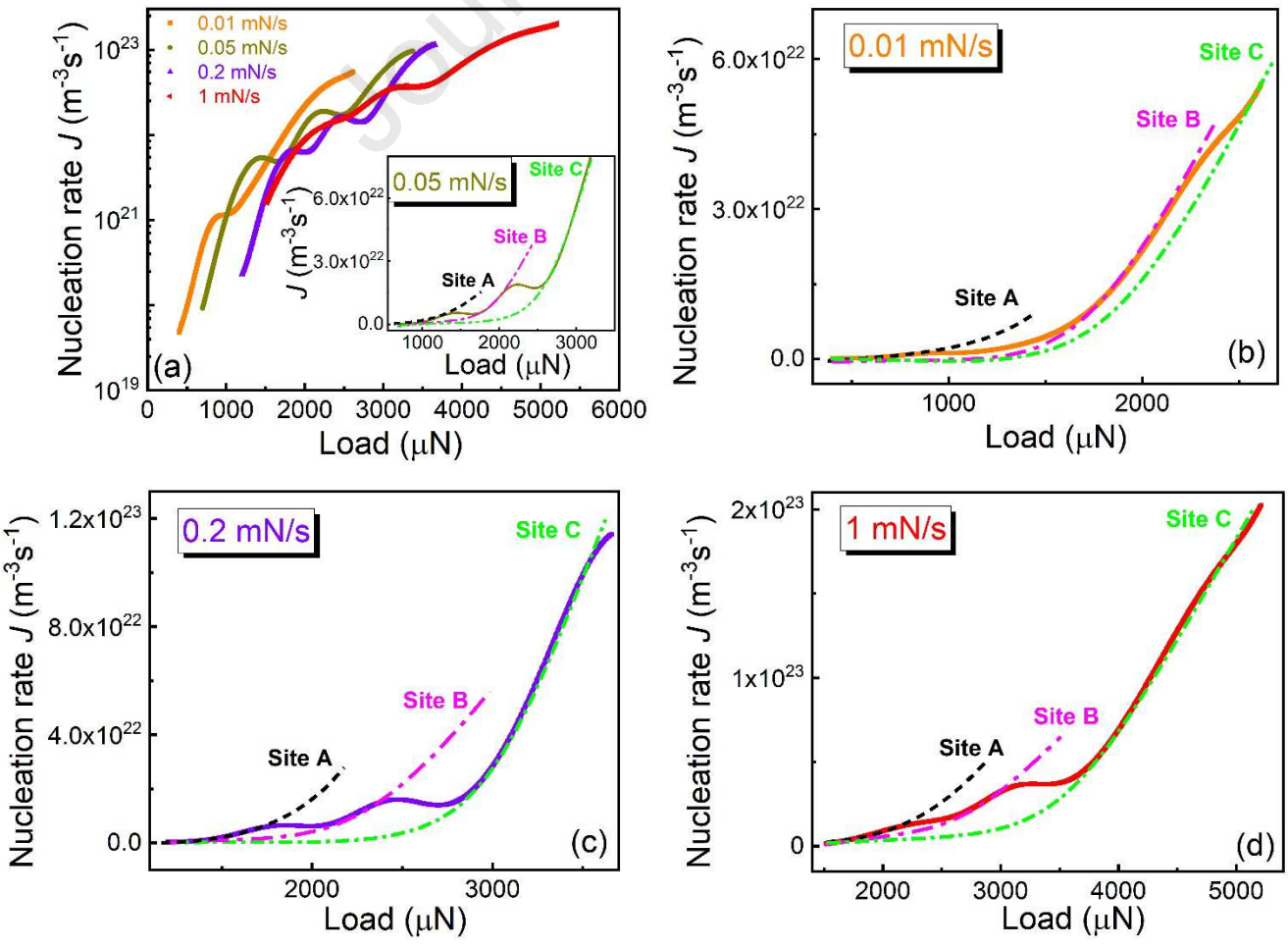

Fig. 6. ***M. Gao et al.***

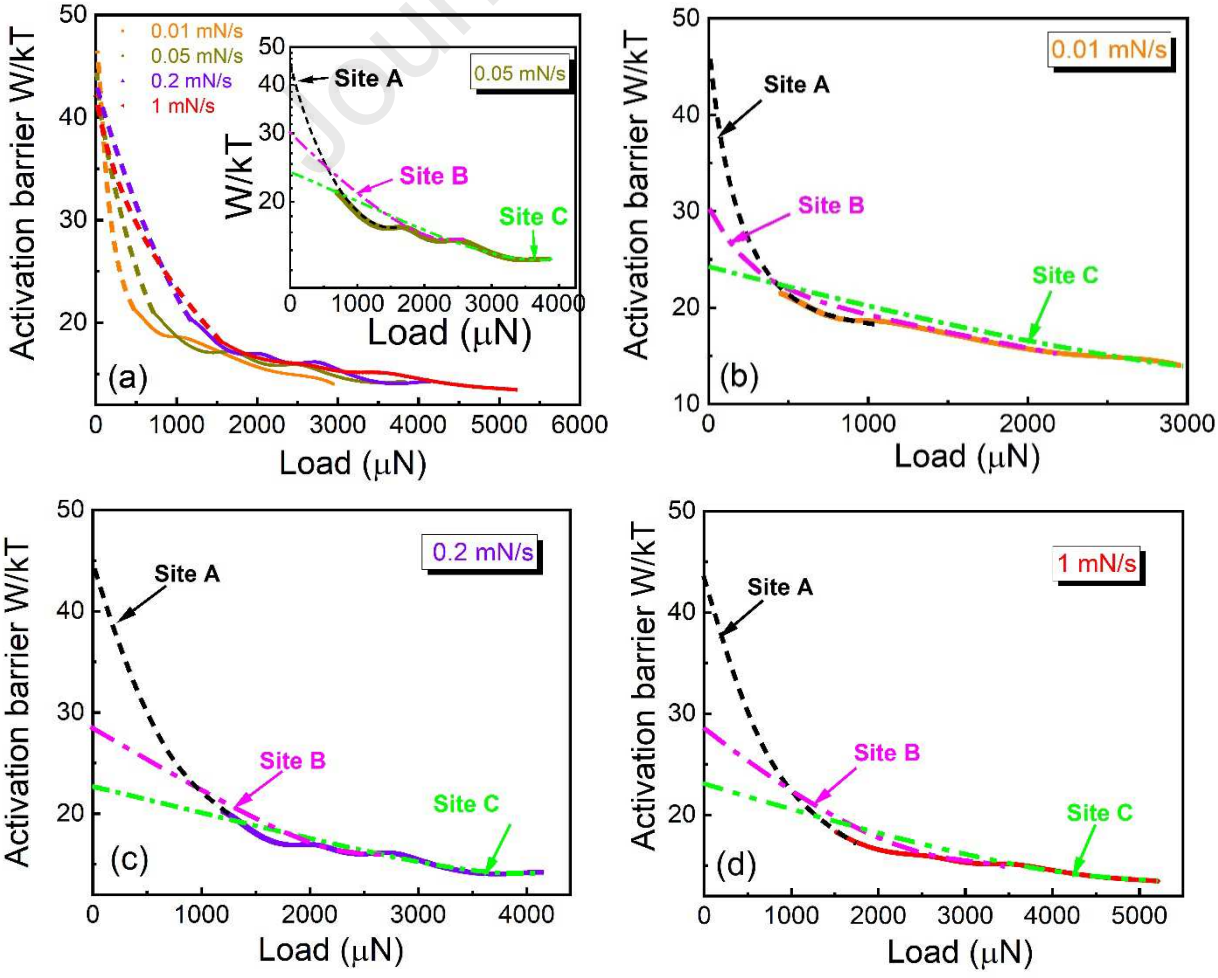

Fig. 7. ***M. Gao et al.***

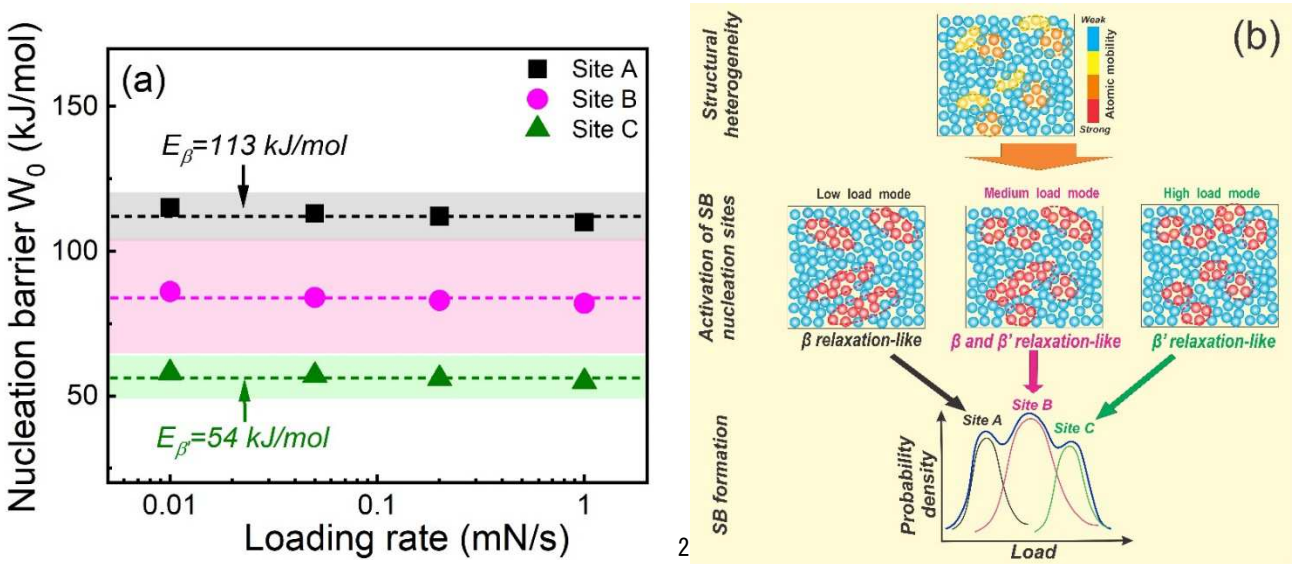

Fig. 8. ***M. Gao et al.***

Tables

Table 1. Summary of physical parameters for $Gd_{55}Co_{25}Al_{20}$ MG sample in this work and the experimental parameters for the instrumental nanoindenter. $Gd_{55}Co_{25}Al_{20}$ MG sample: Glass transition temperature T_g, primary crystallization temperature T_{x1}, Young's modulus E_s, shear modulus G_s, bulk modulus K_s, Poisson's ratio υ_s, reduced elastic modulus E_r. Nanoindenter: Young's modulus E_i, Poisson's ratio υ_i, the radius of the tip R_i. The reduced elastic modulus can be calculated by $E_r = \frac{E_s E_i}{E_i(1-\upsilon_s 2)+E_s(1-\upsilon_i 2)}$.

$Gd_{55}Co_{25}Al_{20}$							Nanoindenter		
T_g	T_{x1}	E_s	G_s	K_s	υ_s	E_r	E_i	υ_i	R_i
590 K	645 K	55.4 GPa	21.2 GPa	47.2 GPa	0.304	58.0 GPa	1140 GPa	0.07	1.10 μm

Table 2. The values of the nucleation barrier W_0 without load for three nucleation sites in Gd-based MG. The values of W_0 are obtained by extrapolating the fitted curves into the external load of 0, as shown in the inserted plot of Fig. 7(a), and Figs. 7(b)-7(d).

W_0 (kJ/mol)	Loading rate (mN/s)			
	0.01	0.05	0.2	1
Site A	114	113	112	112
Site B	85	84	84	83
Site C	57	57	56	56

Highlights:

- An effective strategy by nanoindentation reveal the multiple distribution of shear band nucleation.
- A unique trimodal distribution of shear band nucleation sites in Gd-based MG for the first time.
- The diagram of first pop-in load with loading rates for three nucleation sites were plotted.
- The nucleation sits density, nucleation rate and activation barrier for three nucleation sites were determined.
- The types of shear band nucleation sites are related to the types of characteristic relaxation behavior.

CRediT author statement:

Meng Gao: Conceptualization, Methodology, Investigation, Data curation, Software, Validation, Visulatzation, Writing- Original Draft Preparation. John H. Perepezko: Conceptualization, Supervision, Writing- Reviewing and Editing.

Declaration of interests

☒ The authors declare that they have no known competing financial interests or personal relationships that could have appeared to influence the work reported in this paper.

☐The authors declare the following financial interests/personal relationships which may be considered as potential competing interests: